

# Enhanced Super-rotation Before and During the 2018 Martian Global Dust Storm

Kylash Rajendran<sup>1</sup>, Stephen R. Lewis<sup>1</sup>, James A. Holmes<sup>1</sup>, Paul M. Streeter<sup>1</sup>,  
Anna A. Fedorova<sup>2</sup>, and Manish R. Patel<sup>1,3</sup>

<sup>1</sup>School of Physical Sciences, The Open University, Milton Keynes, UK

<sup>2</sup>Space Research Institute of the Russian Academy of Sciences (IKI RAS), Moscow, Russia

<sup>3</sup>Space Science and Technology Department, Science and Technology Facilities Council,

Rutherford Appleton Laboratory, Oxfordshire, United Kingdom

## Key Points:

- The martian atmosphere was already in a state of enhanced super-rotation prior to the onset of the Mars Year 34 global dust storm
- Super-rotation doubled during the peak of the storm and tropical easterlies were strongly enhanced above 60 km
- Equatorward transport of dust from southern mid-latitudes led to enhanced vertical transport in the tropics in the lead-up to the storm

---

Corresponding author: Kylash Rajendran, [kylash.rajendran@open.ac.uk](mailto:kylash.rajendran@open.ac.uk)

**Abstract**

Super-rotation affects - and is affected by - the distribution of dust in the martian atmosphere. We modelled this interaction during the 2018 global dust storm (GDS) of Mars Year 34 using data assimilation. Super-rotation increased by a factor of two at the peak of the GDS, as compared to the same period in the previous year which did not feature a GDS. A strong westerly jet formed in the tropical lower atmosphere, with strong easterlies above 60 km, as a result of momentum transport by thermal tides. Enhanced super-rotation is shown to have commenced 40 sols before the onset of the GDS, due to equatorward advection of dust from southern mid-latitudes. The uniform distribution of dust in the tropics resulted in a symmetric Hadley cell with a tropical upwelling branch that could efficiently transport dust vertically; this may have significantly contributed to the rapid expansion of the storm.

**Plain Language Summary**

Dust plays a major role in driving the behaviour of the atmosphere of Mars. During a global dust storm, winds lift and transport dust throughout the atmosphere; in turn, dust affects wind direction and strength by heating and cooling the surrounding air. Using a technique that combines satellite observations with simulations of the martian atmosphere, we demonstrate that winds at tropical latitudes were greatly strengthened during the 2018 global dust storm as a result of heating by dust. We show that tropical winds were strengthened even before the onset of the storm, as a result of a dust-driven modification to the tropical circulation pattern. This change in the tropical circulation may have played a role in the formation of the global dust storm.

**1 Introduction**

A planetary atmosphere is said to be in a state of *super-rotation* if the total axial angular momentum of the atmosphere is greater than the angular momentum of an atmosphere in a state of pure solid body rotation (Read, 1986). Super-rotation usually takes the form of an equatorial jet directed in the same sense as the planet's rotation, and it has been shown that such a state can only be maintained by the equatorward transport of angular momentum by non-axisymmetric eddy motions (Hide, 1969). Identifying the exact mechanisms that initiate and maintain super-rotating jets remains a significant challenge in planetary atmospheric research, and is crucial for understanding the atmospheric dynamics of slow-rotating terrestrial planets such as Venus and Titan (Read & Lebonnois, 2018). The Martian atmosphere is also a candidate for super-rotation, as first identified by Lewis and Read (2003).

Global dust storms (GDS) are the most dramatic of all dust-related phenomena in the martian atmosphere, and occur every few martian years. During a GDS, the planet is encircled by a shroud of dust that can persist for several months at a time, drastically affecting the atmospheric state. Such storms have all been observed to occur during the high dust loading season ( $L_S=180^\circ-360^\circ$ ), when the planet's orbit brings it closer to the Sun (Kahre et al., 2017). The formation mechanisms of a GDS are still not well understood; in particular, it has not been established why a GDS forms out of regional storms in some years, but not others. Posited hypotheses include the re-distribution of dust between finite reservoirs between years (Mulholland et al., 2013; Newman & Richardson, 2015), competition between the hemispheric circulations during northern winter (Haberle, 1986), weak coupling between orbital and rotational angular momentum on Mars (Shirley, 2017; Newman et al., 2019) and enhanced surface drag due to constructive interference of tides (Montabone et al., 2008; Martinez-Alvarado et al., 2009).

Lewis and Read (2003) have shown that dust-driven heating can excite a super-rotating jet in the Martian atmosphere. In turn, the strengthening of the equatorial jet

65 by the presence of dust affects dust transport; in this way, there is an intimate link be-  
 66 tween dust-driven heating and the strength of the equatorial jet which may have impli-  
 67 cations for GDS evolution.

68 The most recent GDS occurred in Mars Year (MY) 34 (using the naming conven-  
 69 tion of Clancy et al. (2000)). The storm initiated shortly after the northern hemisphere  
 70 autumn equinox at  $L_S=187^\circ$ , and its dynamical evolution was monitored by multiple or-  
 71 bital, surface and Earth-based instruments, e.g. (Guzewich et al., 2019; Hernández-Bernal  
 72 et al., 2019; Kass et al., 2019; Smith, 2019; Sánchez-Lavega et al., 2019; Shirley et al.,  
 73 2020). Bertrand et al. (2020) simulated the MY34 GDS using the NASA Ames Mars Global  
 74 Climate Model (MGCM) and noted that eastward tropical expansion was a dominant  
 75 feature of both the MY25 and MY34 GDS, highlighting the link between super-rotation  
 76 and dust transport in the early stages of GDS formation. Gillespie et al. (2020) used  
 77 the EMARS reanalysis to study dust encirclement of the northern hemisphere in the early  
 78 stages of the GDS, and showed that a significant portion (16%) of the encirclement could  
 79 be attributed to wind-driven dust advection. Super-rotation during the MY34 GDS was  
 80 further examined by Montabone et al. (2020), who simulated the GDS period using the  
 81 MGCM developed at the Laboratoire de Météorologie Dynamique (LMD). They reported  
 82 a global super-rotation value of  $S = 16\%$  during the peak of the MY34 GDS, as com-  
 83 pared to a pre-dust storm value of 5% (super-rotation metrics are defined in section 2.3).

84 In this paper we perform an analysis of super-rotation during MY33–34, with a spe-  
 85 cial focus on the period leading up to the onset of the MY34 GDS ( $L_S=160^\circ-187^\circ$ ) which  
 86 has not been studied by previous authors. MY33 was used for comparisons as it is an  
 87 adjacent year that did not have a GDS. For this work we analyse the outputs from a data  
 88 assimilation scheme (Lewis et al., 2007) that was used to assimilate temperature and col-  
 89 umn dust data from the Mars Climate Sounder (MCS) and Atmospheric Chemistry Suite  
 90 (ACS) instruments into a MGCM. As data assimilation uses observational data to con-  
 91 strain the evolution of model dynamics, it provides an excellent tool to perform such anal-  
 92 ysis. In Section 2, we describe the satellite observations and give a description of the model  
 93 and assimilation scheme used. We also introduce metrics to quantify super-rotation. We  
 94 document our results in Section 3, and discuss our findings in Section 4.

## 95 2 Data and Methods

### 96 2.1 Observation data

97 MCS is a passive 9-channel limb-scanning radiometer aboard the Mars Reconnaissance  
 98 Orbiter (MRO) (McCleese et al., 2007). Measurements are taken at approximately  
 99 3 am and 3 pm local time along a Sun-synchronous orbit, across a wavelength range of  
 100 0.3–45  $\mu\text{m}$ . Radiance profiles are generated from the surface to around 80 km with an  
 101 intrinsic vertical resolution of 5 km, enabling the retrieval of profiles of temperature, dust  
 102 and water ice (Kleinböhl et al., 2009, 2017). We used version v5.2 for all MCS data out-  
 103 side of the MY34 GDS period. During the GDS period ( $L_S=180^\circ-240^\circ$ ), v5.3.2 was used  
 104 instead, as it extracts additional dust information using a water ice channel. This is pos-  
 105 sible in GDS conditions due to the absence of water ice clouds in the lower atmosphere  
 106 (Montabone et al., 2020).

107 ACS (Korablev et al., 2018) is an array of three infrared spectrometers aboard the  
 108 ExoMars Trace Gas Orbiter (TGO), that together provide spectral coverage over a wave-  
 109 length range of 0.7–17  $\mu\text{m}$ . The near-infrared (NIR) channel uses an echelle grating with  
 110 an Acousto-Optical Tunable filter with a resolving power of 25,000, to retrieve atmospheric  
 111 density and temperature profiles based on the 1.57  $\mu\text{m}$   $\text{CO}_2$  band (Fedorova et al., 2020).  
 112 The orbit of TGO allows for solar occultations that cross the terminator over a range  
 113 of local times, a key feature of these datasets. ACS-NIR temperature profiles were in-  
 114 cluded in our assimilation of MY34 over the period  $L_S=163^\circ-360^\circ$ .

115

## 2.2 Global Climate Model and data assimilation scheme

116

117

118

119

120

121

122

123

124

125

126

The Martian atmosphere is modelled using the UK version of the LMD MGCM (Forget et al., 1999). The model utilises a spectral dynamical core (Hoskins & Simmons, 1975), together with a vertical finite difference scheme that conserves energy and angular momentum (Simmons & Burridge, 1981) and a semi-Lagrangian tracer advection scheme (Newman et al., 2002). Physical processes on Mars are represented using the physics package from the LMD model, which includes schemes for CO<sub>2</sub> condensation and sublimation, radiative transfer, dust transport and boundary layer processes (Forget et al., 1999; Madeleine et al., 2011; Colaïtis et al., 2013) amongst many others. Dust transport is via a radiatively active two-moment scheme that advects the dust mass mixing ratio and number density, which are then used to infer the particle size distribution at each point for radiative transfer calculations (Madeleine et al., 2011).

127

128

129

130

131

132

133

134

The data assimilation scheme is an implementation of the Analysis Correction (AC) scheme, originally developed for terrestrial applications (Lorenc et al., 1991) and later modified and re-tuned for the Martian context (Lewis et al., 1996, 2007). The scheme employs a form of successive corrections, with analysis increments interlaced between dynamical timesteps. It has been successfully employed in assimilating profiles of temperature and column dust opacity from the Thermal Emission Spectrometer (TES) (Lewis & Barker, 2005; Montabone et al., 2005; Lewis et al., 2007) MCS (Steele et al., 2014; Holmes et al., 2019, 2020; Streeter et al., 2020) and ACS (Streeter et al., 2021) instruments.

135

136

137

138

139

140

141

142

143

144

145

146

147

148

We performed the assimilation over MY33–34, and ran the model at T42 spatial resolution (triangular truncation at horizontal wavenumber 42), which corresponds to a physical grid resolution of 3.75°. Fifty-five unevenly-spaced, terrain-following vertical levels were used, with the model top at approximately 110 km. The water cycle was not simulated, in order to isolate the dynamical impact of the dust. Available temperature profiles from the MCS and ACS instruments were assimilated at each timestep, and dust opacity at each model level was rescaled so as to match the total column dust optical depth (CDOD) in the model to MCS observations. Details of the temperature and dust assimilation schemes are given in Lewis et al. (2007) and in the Supplementary Material of Streeter et al. (2020). The inclusion of ACS temperature profiles in the assimilation did not produce any significant changes in the overall structure of the circulation or the strength of the jet during MY34, as compared to an assimilation that only included MCS temperature profiles; this confirms the mutual coherence of the different data sources, and the robustness of the assimilation procedure.

149

## 2.3 Super-rotation metrics

Super-rotation can be quantified by defining a global super-rotation index  $S$  (Lewis & Read, 2003) as

$$S = \frac{\iiint \rho u a \cos \phi dV}{\iiint \rho \Omega a^2 \cos^2 \phi dV} \times 100\%, \quad (1)$$

150

151

152

153

154

155

where  $\rho$  is density,  $u$  is the zonal wind velocity, and  $a$ ,  $\phi$  and  $\Omega$  are the planetary radius, latitude and rotation rate respectively. The volume element is  $dV = a^2 \cos \phi d\lambda d\phi dz$ , where  $\lambda$  and  $z$  are east longitude and geometric height respectively. Each integral is performed over the whole atmospheric volume.  $S$  is a measure of the ratio between the atmospheric and solid-body components of angular momentum;  $S > 0$  only if the atmosphere as a whole has more angular momentum than a pure solid body rotation.

Super-rotation can also be diagnosed by defining a local super-rotation index  $s$  as

$$s = [\bar{m}/\Omega a^2 - 1] \times 100\%. \quad (2)$$

Here  $\bar{m}$  is the zonally averaged value of axial angular momentum  $m$ , which is defined as

$$m = a \cos \phi [\Omega a \cos \phi + u]. \quad (3)$$

156 Whereas  $S$  measures global super-rotation,  $s$  is a measure of its spatial distribution.  $s$   
 157 compares the angular momentum of a ring of fluid at a given latitude and height against  
 158 the angular momentum of an equal-mass fluid ring at rest at the equatorial surface (Read  
 159 & Lebonnois, 2018). Positive values of  $s$  represent local super-rotation.

### 160 3 Results

#### 161 3.1 Atmospheric super-rotation

162 Fig. 1 shows the variation of the global super-rotation metric  $S$  through MY33–34  
 163 (lower panel), along with corresponding equatorial ( $10^\circ\text{N}$ – $10^\circ\text{S}$ ) CDOD values (upper  
 164 panel). The large peak in  $S$  centered at  $L_S=200^\circ$  in MY34 clearly corresponds to the  
 165 mature phase of the GDS (Kass et al., 2019). There are also several smaller local max-  
 166 ima that occur on both curves. The peaks at  $L_S=105^\circ$  in MY33 and  $L_S=135^\circ$  in MY34  
 167 have been identified as spurious and are due to short absences in MCS data availabil-  
 168 ity over those periods. The MY34 curve has additional peaks at  $L_S=175^\circ$  and  $L_S=325^\circ$ .  
 169 The peak at  $L_S=175^\circ$  occurs just prior to the initiation of the GDS, and will be discussed  
 170 further in section 3.3. The peak at  $L_S=325^\circ$  corresponds to the timing of the regional  
 171 ‘C’ storm that occurred late in the year, as can be seen from the concurrent increase in  
 172 CDOD values.

173 Outside of the global dust storm period, the values of  $S$  are broadly similar in both  
 174 years. Global super-rotation variations have a semi-annual structure, with broad peaks  
 175 occurring during equinoxes and troughs occurring during the solstices. These changes  
 176 reflect the changes in the Hadley cell structure over the course of the year (Lewis & Read,  
 177 2003).  $S$  remains largely positive throughout both years of study, except during north-  
 178 ern summer solstice. The average values of  $S$  are 3.4% and 3.9% for MY33 and MY34  
 179 respectively.

#### 180 3.2 Super-rotation during the MY34 GDS

181 The major feature in Fig. 1 is a large peak in  $S$  corresponding to the mature phase  
 182 of the MY34 GDS. Global super-rotation in MY34 first diverges significantly from MY33  
 183 values at  $L_S=165^\circ$ , when the dust opacity in the tropics first begins to increase. After  
 184 an initial peak to  $S = 7.2\%$  at  $L_S=173^\circ$ , global super-rotation increases sharply upon  
 185 storm onset in the Acidalia corridor at  $L_S=187^\circ$ . After reaching a plateau at  $S = 11.3\%$ ,  
 186 the value of  $S$  was boosted again by the onset of intense dust lifting in the Tharsis re-  
 187 gion at  $L_S=197^\circ$  (Bertrand et al., 2020; Montabone et al., 2020), reaching a maximum  
 188 of  $S = 12.6\%$  at  $L_S=201^\circ$ . The peak value is twice as large as the corresponding MY33  
 189 value of  $S = 6.2\%$ , indicating a significant increase in atmospheric angular momentum.  
 190 After the peak,  $S$  decays at a uniform rate, and returns to background values at  $L_S=240^\circ$ .

191 Fig. 2 depicts values of zonal-mean zonal winds and the local super-rotation index  
 192 across latitude and height, during the MY34 GDS period in both years. The data have  
 193 been averaged in time over  $20^\circ$  periods of solar longitude. These broadly cover the ini-  
 194 tiation, peak and decay phases of the storm. In all periods, super-rotation is stronger  
 195 in MY34 than in MY33.

196 In the time period of storm initiation (Figs. 2(a)–(b)), the atmosphere is in an equinoctial  
 197 state. There are extratropical westerly jets in both hemispheres, and easterlies over  
 198 much of the tropics in MY33. There is a substantial difference in tropical wind morphol-  
 199 ogy between the years; this is reflected by the local super-rotation values in the tropics,  
 200 which peak at  $s \approx 12\%$  in MY34 compared to  $s \approx 1\%$  in MY33. Tropical westerlies  
 201 extend up to 50 km in MY34.

202 Super-rotation is strongest in the period  $L_S = 200^\circ - 220^\circ$  of MY34 (Fig. 2(d)),  
 203 which corresponds to the peak of the GDS. The super-rotating jet continues to domi-

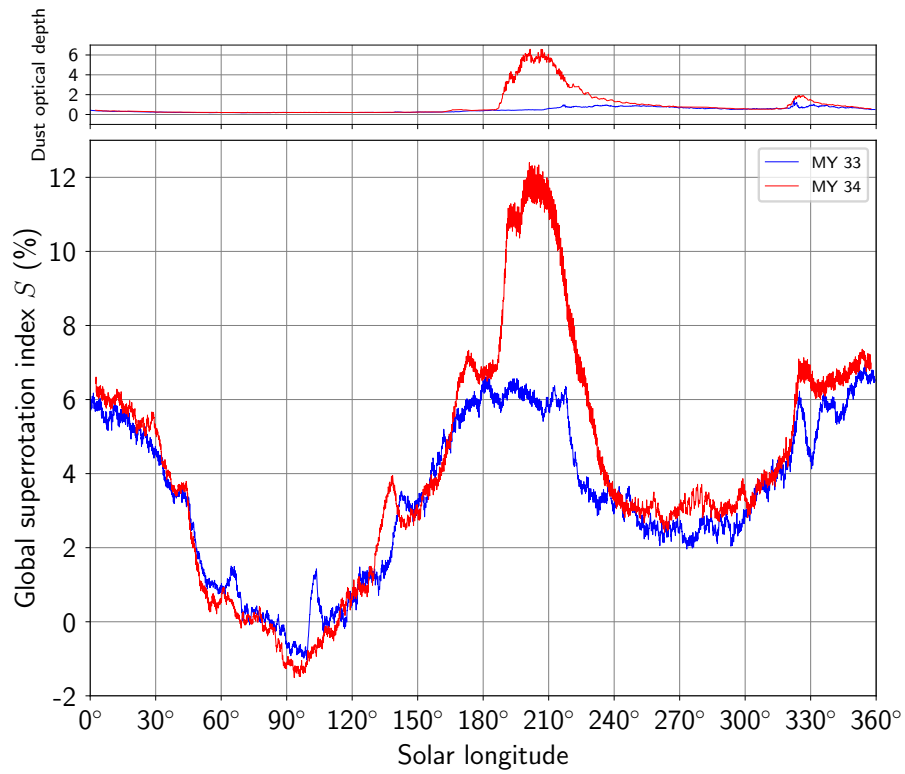


**Figure 1.** Values of the global super-rotation metric  $S$  during MY33 (blue) and MY34 (red). Positive values indicate global super-rotation. The upper panel shows the corresponding zonal mean CDOD values averaged over 10°N–10°S.

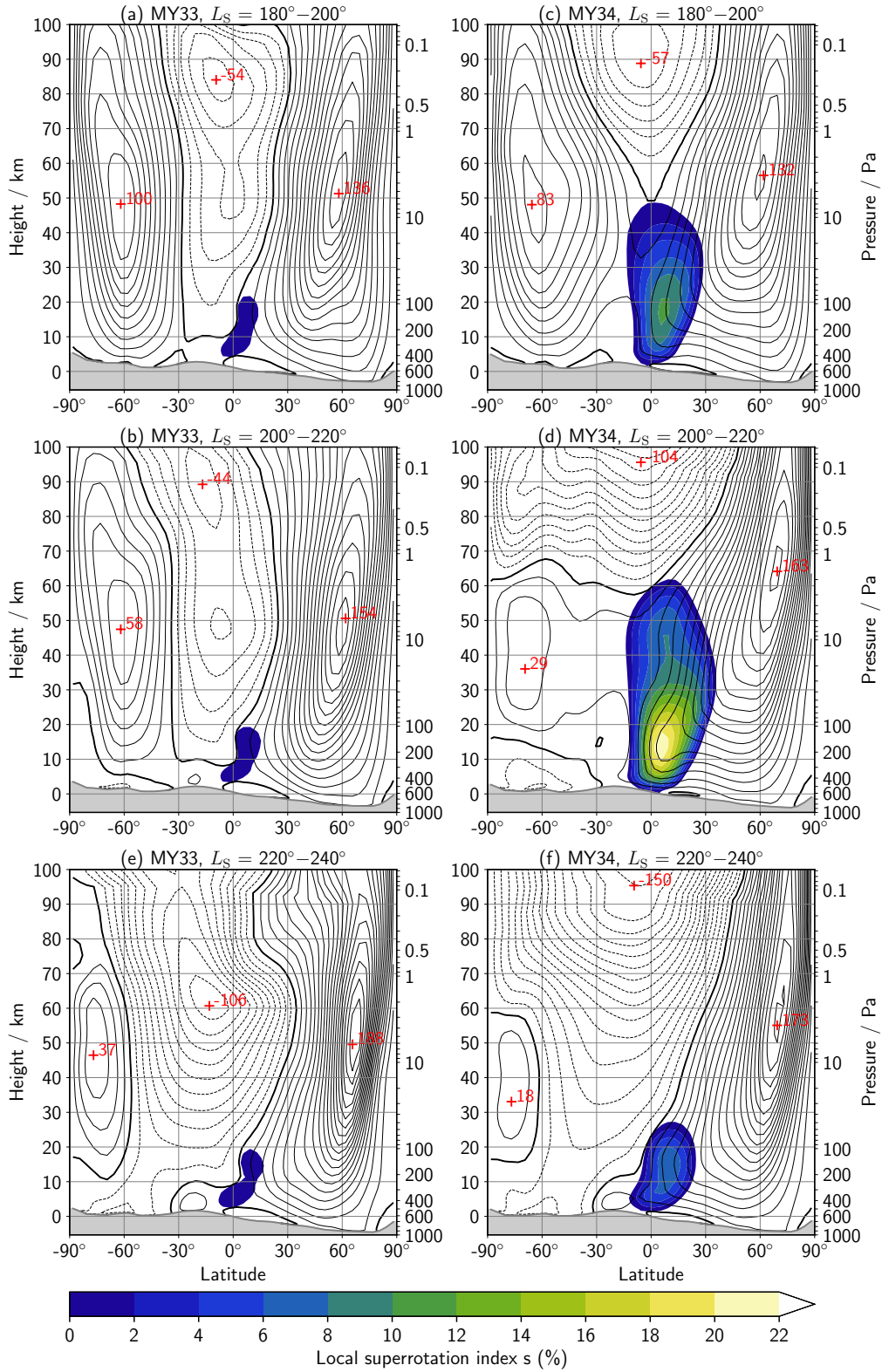


**Figure 2.** Zonal-mean zonal wind (black contours) and local super-rotation index (filled contours) during the MY34 GDS period for MY33 (left) and MY34 (right). Wind contours are drawn at  $10 \text{ m s}^{-1}$  intervals, with westerlies (easterlies) denoted by solid (dashed) contours. The bold solid contour is the zero wind line. Maximal wind values are marked in red.

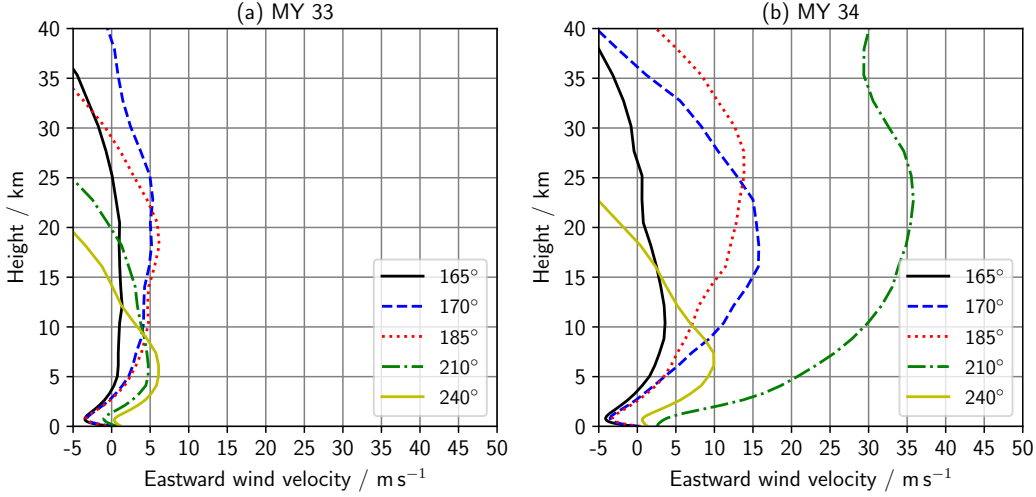


**Figure 3.** Profiles of tropical zonal-mean zonal winds (averaged diurnally and across 30° S – 30° N) for different times during the GDS period for MY33 (left) and MY34 (right).

204 nate the tropical band, and extends up to 60 km. There is a strong peak in local super-  
 205 rotation of  $s = 22\%$  at 20 km, reflecting a significant acceleration of tropical winds by  
 206 the increased dust presence. Easterly winds above 60 km are also enhanced in MY34, and  
 207 increase with height to  $-100 \text{ m s}^{-1}$  near the top of the model. In comparison, tropical  
 208 easterly winds in MY33 peak at  $-40 \text{ m s}^{-1}$  at 50 km, and remain relatively constant at  
 209 higher altitudes (Fig. 2(c)).

210 In the decay phase of the storm (Figs. 2(e)–(f)), easterly winds dominate the tropi-  
 211 cal regions above 20 km and increase monotonically in MY34 to a peak of  $-140 \text{ m s}^{-1}$ .  
 212 Super-rotation is confined to the lower atmosphere below 30 km, and is greatly reduced  
 213 in intensity.

214 Fig. 3 shows the evolution of zonal-mean zonal wind profiles in the tropics over the  
 215 course of the GDS period for MY33 (left) and MY34 (right). Wind profiles at each solar  
 216 longitude were averaged diurnally and between 30° S–30° N.

217 The tropical zonal wind profile does not change substantially between  $L_S=165^\circ$ –  
 218  $210^\circ$  of MY33. Easterly winds in the lowermost atmosphere are overlain by westerly winds  
 219 with velocities of around  $5 \text{ m s}^{-1}$  (Fig. 3(a)). The wind profile for  $L_S=165^\circ$  in MY34 is  
 220 similar to the winds in MY33, but by  $L_S=170^\circ$  zonal wind speeds have increased at al-  
 221 most all heights (Fig. 3(b)). The wind profile weakens slightly at  $L_S=185^\circ$ , before strength-  
 222 ening substantially to reach peak values of  $35 \text{ m s}^{-1}$  at  $L_S=210^\circ$ , with westerly winds pen-  
 223 etrating all the way down to the lowest model level (5 m above the surface). In the de-  
 224 cay phase of the GDS period, wind profiles from MY34 weaken and start to converge with  
 225 profiles from MY33.

### 226 3.3 Atmospheric circulation prior to GDS onset

227 Fig. 4 shows the evolution of the meridional circulation and the dust distribution  
 228 in the assimilation for both years over the period  $L_S=158^\circ$ – $185^\circ$ , prior to GDS initia-  
 229 tion at  $L_S=187^\circ$ . There are no substantive differences between the years at  $L_S=158^\circ$  (Fig. 4(a)–  
 230 (b)). At  $L_S=161^\circ$  in MY34, turbulent dynamics along the southern polar front causes  
 231 a mass of dust from the southern mid-latitudes to be transported northward and to en-

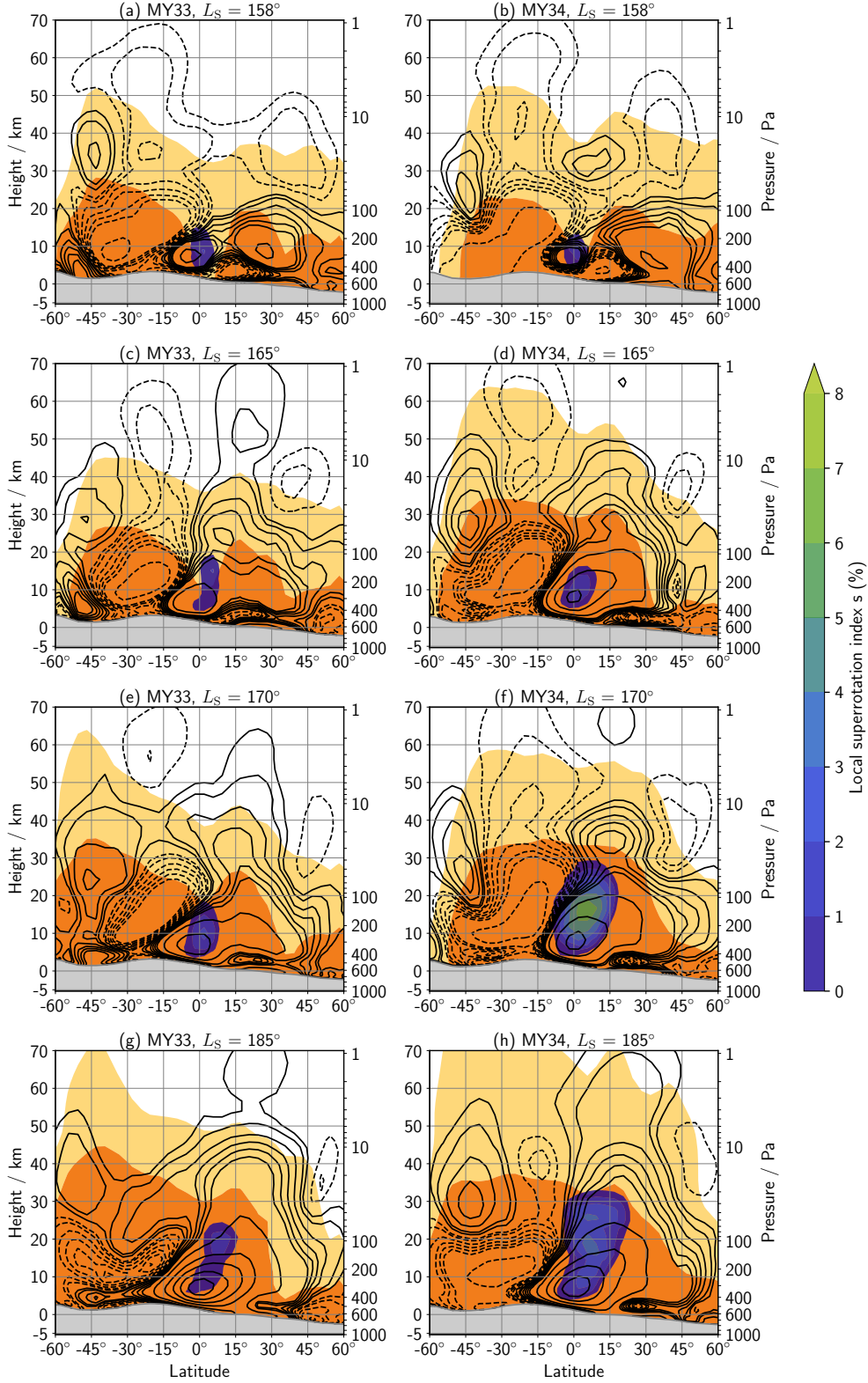


**Figure 4.** Zonal mean dust distribution and dynamical structure at four times (rows) in the lead-up to the GDS for MY33 (left) and MY34 (right). Light (dark) orange shading shows regions of greater than  $1 \times 10^8$  ( $3 \times 10^8$ ) dust particles per kg. Blue-green filled contours indicate the local super-rotation index. Solid (dashed) lines show positive (negative) contours of the mass streamfunction, drawn at  $\pm(0.5, 1, 2, 3, 4, 5, 10, 20, 30, 40, 50) \times 10^8 \text{ kg m}^{-1} \text{ s}^{-1}$ .

232 croach into the tropical region. Some of this dust is entrained into the Hadley cell cir-  
 233 culation and is transported to higher levels in the atmosphere as well as into the north-  
 234 ern hemisphere (Fig. 4(d)). The resulting dust distribution is more uniformly spread across  
 235 tropical latitudes compared to MY33, where the bulk of the dust remains in the south-  
 236 ern hemisphere (Fig. 4(c)).

237 The impact of the different dust distributions on the circulation can be seen in Figs. 4(e)-  
 238 (h). In MY33, dust-driven heating is enhanced in the southern mid-latitudes compared  
 239 to the tropics, causing an inversion of the diabatic heating gradient in the southern hemi-  
 240 sphere between 20–40 km. This weakens the thermally direct circulation in the south-  
 241 ern hemisphere, resulting in the formation of a lopsided Hadley cell with a wavy upwelling  
 242 branch that is less efficient at vertical tracer transport (Figs. 4(e),(g)). In contrast, the  
 243 relatively uniform dust distribution in MY34 engenders a symmetrical Hadley cell with  
 244 an upwelling branch closely aligned to the vertical, as well as enhanced local super-rotation  
 245 (Figs. 4(f),(h)). The circulation patterns in both years do not change substantially be-  
 246 tween  $L_S=170^\circ-185^\circ$ , suggesting that they are relatively stable.

## 247 4 Discussion

248 Our MGCM with data assimilation predicted a peak value of  $S = 12.6\%$  during  
 249 the peak of the storm in MY34, as compared to a value of  $S = 6.3\%$  in MY33 (Fig. 1).  
 250 While the findings are qualitatively similar to those of Montabone et al. (2020), our re-  
 251 sults show that super-rotation increased by a factor of two during the GDS, rather than  
 252 by a factor of three as found by Montabone et al. (2020). This quantitative difference  
 253 between the works can be partly attributed to the impact of temperature assimilation  
 254 in our model, which provides a robust observational constraint on model dynamics.

255 The morphology of tropical winds in our model during the GDS (Fig. 2) is consis-  
 256 tent with the dust-driven enhancement of thermal tides, as explained by Lewis and Read  
 257 (2003). As westward-propagating tides are excited by dust in the lower atmosphere they  
 258 propagate vertically and induce westerly super-rotating winds at their source regions (Fels  
 259 & Lindzen, 1974). Furthermore, the tides eventually break in the upper atmosphere and  
 260 deposit easterly momentum into the background winds, resulting in strengthened east-  
 261 erly flow at higher levels. Such tidally-driven changes in upper atmospheric winds will  
 262 have a significant impact on the distribution of trace species such as water that are trans-  
 263 ported into the upper atmosphere during global dust storms (Fedorova et al., 2018, 2020;  
 264 Aoki et al., 2019). By triggering the breaking levels of gravity waves, these winds also  
 265 play a role in controlling the amount and spectral distribution of gravity waves enter-  
 266 ing the thermosphere, which has implications for water loss as enhanced gravity wave  
 267 activity increases the hydrogen escape flux (Yigit et al., 2021).

268 Enhanced tropical winds played a significant role in the horizontal transport and  
 269 distribution of dust during the initial phase of the GDS (Bertrand et al., 2020; Gillespie  
 270 et al., 2020). We have shown that the martian atmosphere in MY34 was already in a state  
 271 of enhanced super-rotation prior to the onset of the GDS at  $L_S=187^\circ$  (Figs. 1, 2(d), 3,  
 272 4(f)). One consequence of strengthened pre-GDS tropical winds is that eastward dust  
 273 advection during the initial stages of the GDS would have been more rapid in MY34 than  
 274 in years with weaker pre-storm super-rotation. This rapid transport would have enabled  
 275 the timely activation of the secondary Tharsis lifting center, which was crucial in mak-  
 276 ing the dust storm global in extent (Bertrand et al., 2020; Montabone et al., 2020). Fur-  
 277 thermore, we observe that super-rotating winds create regions of enhanced vertical wind  
 278 shear in the lower atmosphere (Fig. 3(b)). As strongly sheared winds are subject to Kelvin-

279 Helmholtz instability, we speculate that jet-induced wind shear could have enhanced the  
 280 generation of turbulence and surface wind stresses prior to the storm. This would lead  
 281 to enhanced dust lifting, especially in the daytime when atmospheric static stability is  
 282 low. However, further work will be required to quantify the impact of such shear-induced  
 283 turbulence on vertical dust transport.

284 Our analysis of the pre-storm circulation indicates that advection of dust from the  
 285 southern mid-latitudes into tropical regions played a key role in inducing the circulation  
 286 pattern of a symmetric Hadley cell with a vertically-aligned tropical upwelling branch  
 287 (Fig. 4). As a result of this pattern, vertical transport was much more efficient in MY34  
 288 in the lead-up to the storm, as compared to MY33. Such a pre-storm circulation pat-  
 289 tern could be an important pre-requisite condition that enabled the rapid lifting of dust  
 290 during GDS initiation (Haberle et al., 1993; Wilson et al., 2008; Shirley et al., 2020). There-  
 291 fore, even though the MY34 GDS is considered to have initiated in the northern hemi-  
 292 sphere (Sánchez-Lavega et al., 2019; Bertrand et al., 2020), our results indicate that dust  
 293 transport from the southern hemisphere may still have played a crucial role in GDS ini-  
 294 tiation.

295 In conclusion, we have conducted a data assimilation study of super-rotation in MY33-  
 296 34. We found that super-rotation increased by a factor of two during the MY34 GDS,  
 297 with substantial changes to tropical wind profiles at all levels. The atmosphere was found  
 298 to have entered a state of super-rotation more than forty sols prior to GDS onset, as a  
 299 result of tropical heating induced by dust transported into the tropics from southern mid-  
 300 latitudes. The resulting uniform redistribution of dust across tropical latitudes resulted  
 301 in a symmetrical Hadley cell circulation with a tropical upwelling branch that was closely  
 302 aligned to the vertical, thereby enhancing the efficiency of vertical transport of dust in  
 303 MY34 and providing conditions conducive to the rapid global-scale expansion of the dust  
 304 storm.

### 305 Acknowledgments

306 KR, SRL, JAH, PMS and MRP acknowledge the support of the UK Space Agency under  
 307 the following grants: ST/R00145X/1 (KR, SRL, MRP), ST/S001405/1 (JAH, SRL,  
 308 MRP), ST/V005332/1 (PMS, SRL, MRP) and ST/V002295/1 (MRP). AAF acknowl-  
 309 edges the subsidy of the Ministry of Science and Higher Education of the Russian Fed-  
 310 eration to IKI RAS (theme ‘Planeta’). PMS acknowledges the support of the STFC un-  
 311 der grant ST/N50421X/1, and the Open University in the form of a PhD studentship.  
 312 Assimilation data from this study may be accessed at <https://figshare.com/s/aa4ee8eab7510d0081dc>.  
 313 ACS raw data products are available from the ESA Planetary Science Archive ([https://](https://archives.esac.esa.int/psa/)  
 314 [archives.esac.esa.int/psa/](https://archives.esac.esa.int/psa/)). MCS data is available from the NASA Planetary Data  
 315 System (<https://pds-atmospheres.nmsu.edu/>).

### 316 References

- 317 Aoki, S., Vandaele, A., Daerden, F., Villanueva, G., Liuzzi, G., Thomas, I., ... oth-  
 318 ers (2019). Water vapor vertical profiles on mars in dust storms observed by  
 319 tgo/nomad. *J. Geophys. Res.-Planet*, *124*(12), 3482–3497.
- 320 Bertrand, T., Wilson, J., Kahre, M., Urata, R., & Kling, A. (2020). Simulation of  
 321 the 2018 global dust storm on mars using the nasa ames mars gcm: A multi-  
 322 tracer approach. *J. Geophys. Res.-Planet*, e2019JE006122.
- 323 Clancy, R., Sandor, B., Wolff, M., Christensen, P., Smith, M., Pearl, J., ... Wilson,  
 324 R. (2000). An intercomparison of ground-based millimeter, mgs tes, and viking  
 325 atmospheric temperature measurements: Seasonal and interannual variability  
 326 of temperatures and dust loading in the global mars atmosphere. *J. Geophys.*  
 327 *Res.-Planet*, *105*(E4), 9553–9571.
- 328 Colaitis, A., Spiga, A., Hourdin, F., Rio, C., Forget, F., & Millour, E. (2013). A

- 329 thermal plume model for the martian convective boundary layer. *J. Geophys.*  
 330 *Res.-Planet*, 118(7), 1468–1487.
- 331 Fedorova, A., Bertaux, J., Betsis, D., Montmessin, F., Korablev, O., Maltagliati, L.,  
 332 & Clarke, J. (2018). Water vapor in the middle atmosphere of mars during the  
 333 2007 global dust storm. *Icarus*, 300, 440–457.
- 334 Fedorova, A., Montmessin, F., Korablev, O., Luginin, M., Trokhimovskiy, A.,  
 335 Belyaev, D., ... others (2020). Stormy water on mars: The distribution and  
 336 saturation of atmospheric water during the dusty season. *Science*, 367(6475),  
 337 297–300.
- 338 Fels, S., & Lindzen, R. (1974). The interaction of thermally excited gravity waves  
 339 with mean flows. *Geophys. Astro. Fluid.*, 6(2), 149–191.
- 340 Forget, F., Hourdin, F., Fournier, R., Hourdin, C., Talagrand, O., Collins, M., ...  
 341 Huot, J. (1999). Improved general circulation models of the martian atmo-  
 342 sphere from the surface to above 80 km. *J. Geophys. Res.-Planet*, 104(E10),  
 343 24155–24175.
- 344 Gillespie, H., Greybush, S., & Wilson, R. (2020). An investigation of the encir-  
 345 clement of mars by dust in the 2018 global dust storm using emars. *J. Geo-*  
 346 *phys. Res.-Planet*, 125(7), e2019JE006106.
- 347 Guzewich, S., Lemmon, M., Smith, C., Martínez, G., de Vicente-Retortillo, Á.,  
 348 Newman, C., ... others (2019). Mars science laboratory observations of the  
 349 2018/mars year 34 global dust storm. *Geophys. Res. Lett.*, 46(1), 71–79.
- 350 Haberle, R. (1986). Interannual variability of global dust storms on mars. *Science*,  
 351 234(4775), 459–461.
- 352 Haberle, R., Pollack, J., Barnes, J., Zurek, R., Leovy, C., Murphy, J., ... Schaeffer,  
 353 J. (1993). Mars atmospheric dynamics as simulated by the nasa ames general  
 354 circulation model: 1. the zonal-mean circulation. *J. Geophys. Res.-Planet*,  
 355 98(E2), 3093–3123.
- 356 Hernández-Bernal, J., Sánchez-Lavega, A., del Río-Gaztelurrutia, T., Hueso, R.,  
 357 Cardesín-Moinelo, A., Ravanis, E., ... Wood, S. (2019). The 2018 martian  
 358 global dust storm over the south polar region studied with mex/vmc. *Geophys.*  
 359 *Res. Lett.*, 46(17-18), 10330–10337.
- 360 Hide, R. (1969). Dynamics of the atmospheres of the major planets with an ap-  
 361 pendix on the viscous boundary layer at the rigid bounding surface of an  
 362 electrically-conducting rotating fluid in the presence of a magnetic field. *J.*  
 363 *Atmos. Sci.*, 26(5), 841–853.
- 364 Holmes, J., Lewis, S., & Patel, M. (2020). Openmars: A global record of martian  
 365 weather from 1999–2015. *Planet. Space Sci.*, 104962.
- 366 Holmes, J., Lewis, S., Patel, M., & Smith, M. (2019). Global analysis and forecasts  
 367 of carbon monoxide on mars. *Icarus*, 328, 232–245.
- 368 Hoskins, B., & Simmons, A. (1975). A multi-layer spectral model and the semi-  
 369 implicit method. *Q. J. Roy. Meteo. Soc.*, 101(429), 637–655.
- 370 Kahre, M., Murphy, J., Newman, C., Wilson, R., Cantor, B., Lemmon, M., &  
 371 Wolff, M. (2017). The mars dust cycle. In R. Haberle, R. Clancy, F. Forget,  
 372 M. Smith, & R. Zurek (Eds.), *The atmosphere and climate of mars*  
 373 (p. 295–337). Cambridge University Press. doi: 10.1017/9781139060172.010
- 374 Kass, D., Schofield, J., Kleinböhl, A., McCleese, D., Heavens, N., Shirley, J., &  
 375 Steele, L. (2019). Mars climate sounder observation of mars’ 2018 global dust  
 376 storm. *Geophys. Res. Lett.*
- 377 Kleinböhl, A., Friedson, A., & Schofield, J. (2017). Two-dimensional radiative trans-  
 378 fer for the retrieval of limb emission measurements in the martian atmosphere.  
 379 *J. Quant. Spectrosc. Ra.*, 187, 511–522.
- 380 Kleinböhl, A., Schofield, J., Kass, D., Abdou, W., Backus, C., Sen, B., ... others  
 381 (2009). Mars climate sounder limb profile retrieval of atmospheric temper-  
 382 ature, pressure, and dust and water ice opacity. *J. Geophys. Res.-Planet*,  
 383 114(E10).

- 384 Korablev, O., Montmessin, F., Trokhimovskiy, A., Fedorova, A., Shakun, A., Grig-  
 385 oriev, A., . . . others (2018). The atmospheric chemistry suite (acs) of three  
 386 spectrometers for the exomars 2016 trace gas orbiter. *Space Sci. Rev.*, *214*(1),  
 387 7.
- 388 Lewis, S., & Barker, P. (2005). Atmospheric tides in a mars general circulation  
 389 model with data assimilation. *Adv. Space Res.*, *36*(11), 2162–2168.
- 390 Lewis, S., & Read, P. (2003). Equatorial jets in the dusty martian atmosphere. *J.*  
 391 *Geophys. Res.-Planet*, *108*(E4).
- 392 Lewis, S., Read, P., & Collins, M. (1996). Martian atmospheric data assimila-  
 393 tion with a simplified general circulation model: Orbiter and lander networks.  
 394 *Planet. Space Sci.*, *44*(11), 1395–1409.
- 395 Lewis, S., Read, P., Conrath, B., Pearl, J., & Smith, M. (2007). Assimilation of ther-  
 396 mal emission spectrometer atmospheric data during the mars global surveyor  
 397 aerobraking period. *Icarus*, *192*(2), 327–347.
- 398 Lorenc, A., Bell, R., & Macpherson, B. (1991). The meteorological office analysis  
 399 correction data assimilation scheme. *Q. J. Roy. Meteo. Soc.*, *117*(497), 59–89.
- 400 Madeleine, J., Forget, F., Millour, E., Montabone, L., & Wolff, M. (2011). Revisiting  
 401 the radiative impact of dust on mars using the lmd global climate model. *J.*  
 402 *Geophys. Res.-Planet*, *116*(E11).
- 403 Martinez-Alvarado, O., Montabone, L., Lewis, S., Moroz, I., & Read, P. (2009).  
 404 Transient teleconnection event at the onset of a planet-encircling dust storm  
 405 on mars. *Ann. Geophys*, *27*(9), 3663–3676.
- 406 McCleese, D., Schofield, J., Taylor, F., Calcutt, S., Foote, M., Kass, D., . . . Zurek,  
 407 R. (2007). Mars climate sounder: An investigation of thermal and water vapor  
 408 structure, dust and condensate distributions in the atmosphere, and energy  
 409 balance of the polar regions. *J. Geophys. Res.-Planet*, *112*(E5).
- 410 Montabone, L., Lewis, S., & Read, P. (2005). Interannual variability of martian dust  
 411 storms in assimilation of several years of mars global surveyor observations.  
 412 *Adv. Space Res.*, *36*(11), 2146–2155.
- 413 Montabone, L., Martinez-Alvarado, O., Lewis, S., Read, P., & Wilson, R. (2008).  
 414 Teleconnection in the martian atmosphere during the 2001 planet-encircling  
 415 dust storm. In *Third international workshop on the mars atmosphere: Model-*  
 416 *ing and observations* (Vol. 1447, p. 9077).
- 417 Montabone, L., Spiga, A., Kass, D., Kleinböhl, A., Forget, F., & Millour, E. (2020).  
 418 Martian year 34 column dust climatology from mars climate sounder observa-  
 419 tions: Reconstructed maps and model simulations. *J. Geophys. Res.-Planet*,  
 420 e2019JE006111.
- 421 Mulholland, D., Read, P., & Lewis, S. (2013). Simulating the interannual variability  
 422 of major dust storms on mars using variable lifting thresholds. *Icarus*, *223*(1),  
 423 344–358.
- 424 Newman, C., Lee, C., Mischna, M., Richardson, M., & Shirley, J. (2019). An initial  
 425 assessment of the impact of postulated orbit-spin coupling on mars dust storm  
 426 variability in fully interactive dust simulations. *Icarus*, *317*, 649–668.
- 427 Newman, C., Lewis, S., Read, P., & Forget, F. (2002). Modeling the martian dust  
 428 cycle, 1. representations of dust transport processes. *J. Geophys. Res.-Planet*,  
 429 *107*(E12), 6–1.
- 430 Newman, C., & Richardson, M. (2015). The impact of surface dust source exhaus-  
 431 tion on the martian dust cycle, dust storms and interannual variability, as  
 432 simulated by the marswrf general circulation model. *Icarus*, *257*, 47–87.
- 433 Read, P. (1986). Super-rotation and diffusion of axial angular momentum: I. ‘speed  
 434 limits’ for axisymmetric flow in a rotating cylindrical fluid annulus. *Q. J. Roy.*  
 435 *Meteo. Soc.*, *112*(471), 231–251.
- 436 Read, P., & Lebonnois, S. (2018). Superrotation on venus, on titan, and elsewhere.  
 437 *Annu. Rev. Earth Pl. Sc.*, *46*, 175–202.
- 438 Sánchez-Lavega, A., del Río-Gaztelurrutia, T., Hernández-Bernal, J., & Delcroix, M.

- 439 (2019). The onset and growth of the 2018 martian global dust storm. *Geophys.*  
440 *Res. Lett.*, *46*(11), 6101–6108.
- 441 Shirley, J. (2017). Orbit-spin coupling and the circulation of the martian atmo-  
442 sphere. *Planet. Space Sci.*, *141*, 1–16.
- 443 Shirley, J., Kleinböhl, A., Kass, D., Steele, L., Heavens, N., Suzuki, S., . . . McCleese,  
444 D. (2020). Rapid expansion and evolution of a regional dust storm in the aci-  
445 dalia corridor during the initial growth phase of the martian global dust storm  
446 of 2018. *Geophysical Research Letters*, *47*(9), e2019GL084317.
- 447 Simmons, A., & Burridge, D. (1981). An energy and angular-momentum conserving  
448 vertical finite-difference scheme and hybrid vertical coordinates. *Mon. Weather*  
449 *Rev.*, *109*(4), 758–766.
- 450 Smith, M. (2019). Themis observations of the 2018 mars global dust storm. *J. Geo-*  
451 *phys. Res.-Planet*, *124*(11), 2929–2944.
- 452 Steele, L., Lewis, S., Patel, M., Montmessin, F., Forget, F., & Smith, M. (2014). The  
453 seasonal cycle of water vapour on mars from assimilation of thermal emission  
454 spectrometer data. *Icarus*, *237*, 97–115.
- 455 Streeter, P., Lewis, S., Patel, M., Holmes, J., Fedorova, A., Kass, D., & Kleinböhl,  
456 A. (2021). Asymmetric impacts on mars’ polar vortices from an equinoctial  
457 global dust storm. *J. Geophys. Res.-Planet*, e2020JE006774.
- 458 Streeter, P., Lewis, S., Patel, M., Holmes, J., & Kass, D. (2020). Surface warming  
459 during the 2018/mars year 34 global dust storm. *Geophys. Res. Lett.*, *47*(9),  
460 e2019GL083936.
- 461 Wilson, R., Haberle, R., Noble, J., Bridger, A., Schaeffer, J., Barnes, J., & Can-  
462 tor, B. (2008). Simulation of the 2001 planet-encircling dust storm with the  
463 nasa/noaa mars general circulation model. In *Third international workshop on*  
464 *the mars atmosphere: Modeling and observations* (Vol. 1447, p. 9023).
- 465 Yiğit, E., Medvedev, A., Benna, M., & Jakosky, B. (2021). Dust storm-enhanced  
466 gravity wave activity in the martian thermosphere observed by maven and im-  
467 plication for atmospheric escape. *Geophys. Res. Lett.*, *48*(5), e2020GL092095.